Nonlinear Modelling and Simulation of Vibrocompaction Processes

Javier González-Carbajal, Daniel García-Vallejo, Jaime Domínguez

Department of Mechanical and Manufacturing Engineering, University of Seville. C/ Camino de los Descubrimientos s/n, Isla de la Cartuja. 41092 Seville, Spain

e – mail: jgcarbajal@us.es, dgvallejo@us.es, jaime@us.es

Abstract

This paper considers a kind of industrial process where a granular material is compacted by using vibration machines. In particular, attention is focused on the vibrocompaction of quartz agglomerates, where the vibration is produced by rotation of unbalanced electric motors. A four degree-of-freedom nonlinear model, which includes contact and impacts, is proposed to predict the behaviour of the system under study. A relevant aspect of the model is the introduction of a nonlinear, yet relatively simple, constitutive law for the compacting material, which is able to capture the essential features of compaction. The main usefulness of the proposed model is to investigate how different parameters of the industrial process affect the final level of compaction achieved, as is illustrated by numerically solving the equations of motion for several sets of parameter values.

Keywords Vibrocompaction · Nonideal Excitation · Unbalanced Motor · Nonlinear Constitutive Law

---

1. Introduction

Vibrating machines are extensively used as a means to compact granular materials, with applications in geotechnics, manufacturing and other engineering areas. In particular, this paper has been motivated by the interest of the authors in a particular manufacturing process, where a quartz-resin mixture is compacted by using the vibration produced by a set of unbalanced motors, together with a vacuum system.

1.1 The Vibrocompaction of Quartz Agglomerates

Quartz agglomerates, made of granulated quartz mixed with a polyester resin, are widely used as an artificial stone for countertops in kitchens or bathrooms. The manufacturing process of a slab of this material starts with the filling of a mould with the mixture of quartz and resin. Once the mould is full, a conveyor belt carries it to the vibrocompaction zone, where the thickness of the slab is reduced to nearly half of its initial value, by eliminating the air out of the material. The final phases of the process include the polymerization of the resin in a kiln and the cooling and machining of the slab.

It is worth giving some more insight into the vibrocompaction stage of the process, which is the one of interest for the purpose of this study. Before the mixture has been compacted, it is composed of three different phases: solid (the quartz grains), liquid (the resin) and gas (air). The air is present in the material in two different ways: as bubbles within the resin or as gaps between grains of quartz that the resin has not been able to fill. The aim of the compaction process is to eliminate the air out of the mixture, since the presence of pores at the surface of the final countertop is clearly detrimental from a practical point of view: the pores tend to accumulate dirt and are rather difficult to clean.

The compaction is conducted by means of several unbalanced electric motors, mounted on a piston with the dimensions of the slab surface. At the beginning of the vibrocompaction process, the piston descends onto the mixture and exerts a static pressure, due to its weight and to an air pressure applied on it. Then, the air pressure inside the mould is reduced by using a vacuum system, after which the motors are switched on. The vibration produced by the unbalanced motors is the main responsible for the compaction. During the motion of the system, there can be separations and impacts between the piston and the slab, which are generally beneficial for the compaction, as they produce very high peaks of compression forces. It is interesting to note that the motors are mounted in couples which rotate in opposite directions in order to cancel the horizontal components of the centrifugal forces on the unbalanced masses. Hence the net effect of the rotation of both motors is an oscillating vertical force.

From the above comments, it is clear that the vibrocompaction process is extremely complex from a physical point of view. A large number of factors –some of them being intrinsically nonlinear– influence the final result of the compaction: the quartz granulometry, the rheological properties of the resin, the dynamic properties of the different elements of the machine, the speed of the motors, their available power, the amount of unbalance, etc.

1.2 Nonideal Excitations and Sommerfeld Effect

In addition to the mentioned sources of nonlinearity, it is known that, when a structure is excited by one or more unbalanced motors, some particular nonlinear effects can take place due to the interaction itself between the exciter and the vibrating system [1–4]. The main idea is that, in general, the motion of the unbalanced motor will be influenced by the response of the vibrating system, due to the inertia forces that the vibration produces on the unbalanced mass [4]. Then, rather than a known excitation acting on the vibrating system, what we

generally have is a two-way coupling between the motions of the exciter and the structure. In most of the scientific literature, this is called a *nonideal* excitation [5–7], and the associated nonlinear phenomena are usually referred to as *The Sommerfeld effect* [8–10]. Conversely, an excitation is said to be *ideal* if it remains unaffected by the vibrating response.

In 1904, Sommerfeld [11], whose pioneering work inspired many subsequent investigations, found experimentally kinds of behaviour which could not be explained upon the ideality hypothesis. He mounted an unbalanced electric motor on an elastically supported table, as schematically represented in Fig. 1, and monitored the input power as well as the frequency and amplitude of the response [12].

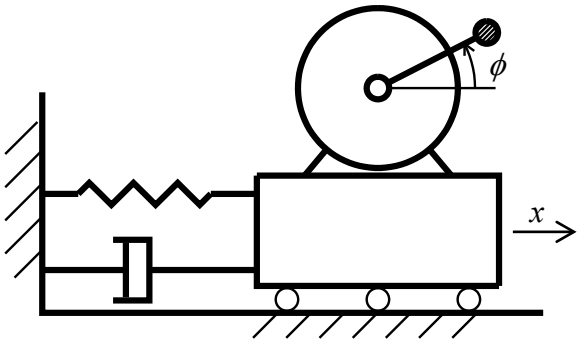

Fig. 1 Simplified representation of the setup for Sommerfeld's experiment

The experiment consisted in increasing continuously the power input in order to make the rotor speed pass through the resonance frequency of the table, and then conduct the inverse process by decreasing the input power. The results obtained by Sommerfeld are qualitatively depicted in Fig. 2. When the rotor speed was close to resonance, an increment of the input power produced only a very slight increase of the rotor speed, while the oscillation amplitude increased considerably. This means that, in this part of the experiment, the increasing input power was not making the motor rotate faster, but was giving rise to larger oscillations. With further increasing of the input power, the rotor speed jumped abruptly to a frequency above resonance and, at the same time, the vibration amplitude jumped to a much smaller quantity than measured in the resonance region. When the process was reversed, by decreasing the motor input power, a jump phenomenon in the resonance region was also observed (see Fig. 2). However, this jump was found to be different to the one obtained for increasing rotor speed.

In 1969, Kononenko [1] published a book entirely devoted to the study of nonideal excitations. He considered different configurations of vibrating systems excited by nonideal motors and applied the Averaging Method [13] to the equations of motion. By taking into account the two-way interaction between the motor and the vibrating structure, he was able to explain the Sommerfeld effect. Konenko showed that the behaviour of the system could be understood by using torque-speed curves. Actually, it was demonstrated in [1] that the stationary motions of the system could be found as the intersections between the torque-speed curve of the motor $L_m(\dot{\phi})$ –or motor characteristic– and a particular curve $L_v(\dot{\phi})$ representing the torque on the rotor due to vibration (see Fig. 3). In other words, the torque generated by the motor needs to equal the resisting torque

produced by the system vibration, in accordance with physical intuition. It is relevant to note that this kind of representation gives a clear explanation for the Sommerfeld Effect.

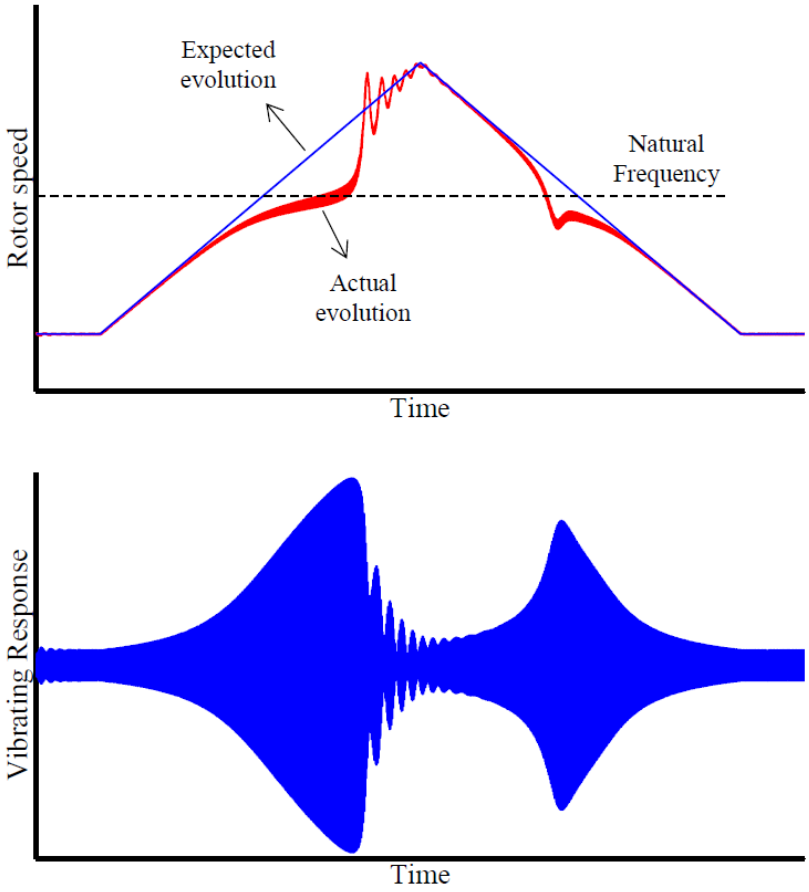

Fig. 2 Sommerfeld Effect

Suppose that the motor is controlled by displacing its characteristic parallel to itself. This is actually the case, for instance, in simplest control approach for an induction motor, known as the V/f control [14]. Then, for increasing (decrasing) input power, the motor curve is displaced upwards (downwards). Consider the first part of Sommerfeld's experiment, where the input power is increased so as to make the rotor speed pass through the system natural frequency. As depicted in Fig. 3, when the system approaches resonance, the increase in the rotor speed is slowed down due to the presence of the resonance peak. This occurs until the motor curve becomes tangent to the vibration torque curve. At this point, the large-amplitude stationary motion disappears through a saddle-node bifurcation, as discussed by Kononenko [1], Dimentberg [3] and others [2,5,9].

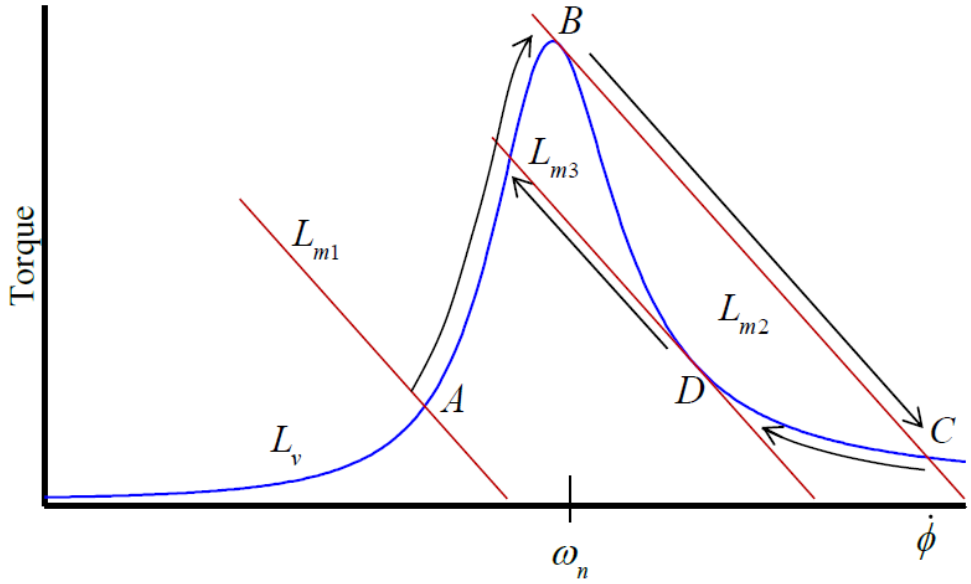

Fig. 3 Explanation of the Sommerfeld Effect

Curves L_{mi} represent the motor characteristics, while L_v corresponds to the torque on the rotor due to vibration

The referred bifurcation makes the system jump towards the only remaining stationary motion, which is a post-resonant state with smaller vibration amplitude. A similar phenomenon takes place for decreasing frequency, although the jump is smaller in this case (see Fig. 3). This classical explanation is in accordance with the analyses given in [1,3,7,9].

Note that, in the above discussion, it is assumed that every solution between A and B, and between C and D, is stable. If the motion of the system lost its stability before the tangency point B or D, then the jump phenomenon would occur before than predicted in Fig. 3. Actually, it was shown in [4,15] that some points between C and D can be unstable. This means that, in the second part of Sommerfeld's experiment (going from C to D in Fig. 3, the jump phenomenon can occur before reaching the tangency point D.

After the works of Sommerfeld and Kononenko, many investigations have been conducted in order to better understand and predict the effect of nonideal excitations on vibrating systems.

Rand et al. [16] reported the detrimental effect of a nonideal energy source in dual spin spacecrafts, which could endanger a particular manoeuvre of the spacecraft, once placed in orbit. They also designed suitable nonlinear controllers to minimize this kind of undesired channelling of energy [17].

Although most studies use averaging procedures to obtain approximate solutions to the equations of motion, Blekhman [2] proposed an alternative approach, based on the method of 'Direct Separation of Motions'.

Several authors, like El-Badawi [9], Bolla et al. [7] and González-Carbajal et al. [4,15], analysed models where the vibrating system included an intrinsic cubic nonlinearity, in addition to the nonlinearity associated to the nonideal coupling between exciter and structure.

Balthazar et al. [5] published an extensive exposition of the state of the art concerning nonideal excitations.

Considering the vibrocompacting machine for quartz agglomerates, it is reasonable to expect that nonlinear effects, produced by a nonideal coupling between the vibrating system and the unbalanced motors, are present in the system behaviour. The model presented in this paper will allow showing how these phenomena, associated to nonideality of the energy source, can affect the result of the compaction process.

The article is organized as follows. Section 2 presents and justifies the nonlinear model for the vibrocompacting system. In Section 3, a number of simulations are conducted in order to illustrate the capabilities of the model as a means of revealing how different parameters of the process influence the result of the compaction. Moreover, the results of the simulations will highlight the way in which the Sommerfeld effect can affect the process under study. Finally, the conclusions of the work are summarized in Section 4.

2. Proposed Model

Building a reliable model of the vibrocompaction process, able to accurately predict the result of the compaction depending on the system parameters, is an extremely hard task, which clearly exceeds the scope of this paper. It should be noted that, as far as the authors know, such a model is not available yet.

The aim of this Section is to present an approximate model which, without intending to give accurate quantitative predictions, provides useful qualitative results regarding the vibrocompaction process. This may be seen as a first step towards the ambitious goal of achieving a more complex model which reliably captures the dynamics of the real system.

The simplification carried out can be observed in Fig. 4 and Fig. 5. The former shows a schematic picture of the real machine, while the later displays the approximate 4-DOF model. The quartz-resin mixture is represented in the model by a couple of masses attached to each other by a linear damper and a nonlinear spring, which models the compaction itself by allowing for permanent deformation when the spring is compressed. Then, the distance between both masses would represent the thickness of the compacting mixture. The mould is modelled as a rigid base, while the piston with the unbalanced motors is represented by a mass with a single unbalanced motor. The mixture is in contact –with separations and impacts allowed– with the mould at the bottom and with the piston at the top. The vacuum system is not included in the model. It should be noted that the model assumes the horizontal motion of the piston to be completely restrained, which makes unnecessary to include a couple of motors rotating in opposite directions.

As represented in Fig. 5, the model has 4 DOFs: y_b, y_t, y_p and ϕ, which correspond, respectively, to position of the bottom of the mixture, position of the top of the mixture, position of the piston and rotation of the motor.

The parameters represented in Fig. 5 are as follows: m_m stands for the mass of the mixture, m_1 is the unbalanced mass, m_p is the mass of the piston and the motor, r is the eccentricity of the unbalance, I_o is the rotor inertia, b is the damping coefficient, F_m is the force produced by the nonlinear spring and g is the gravity constant.

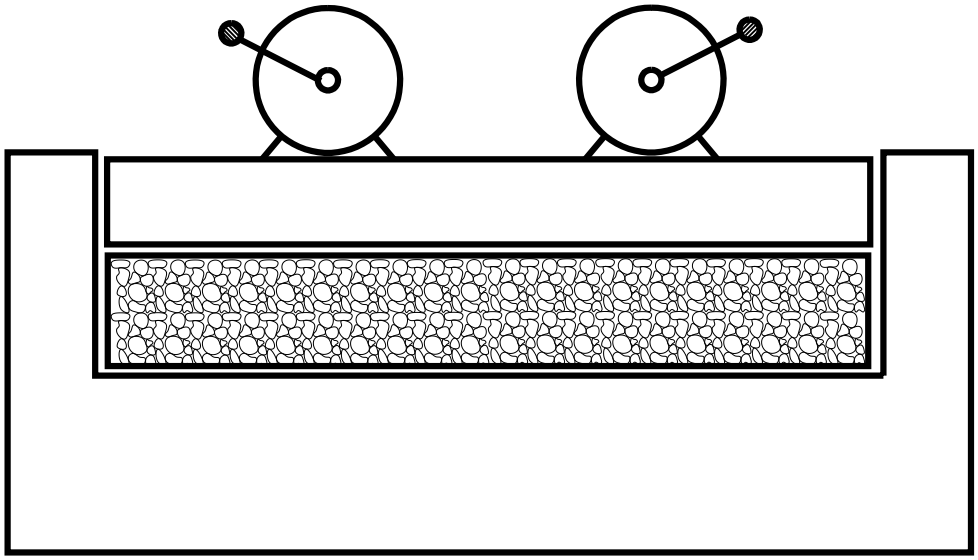

Fig. 4 Simplified representation of the compacting machine

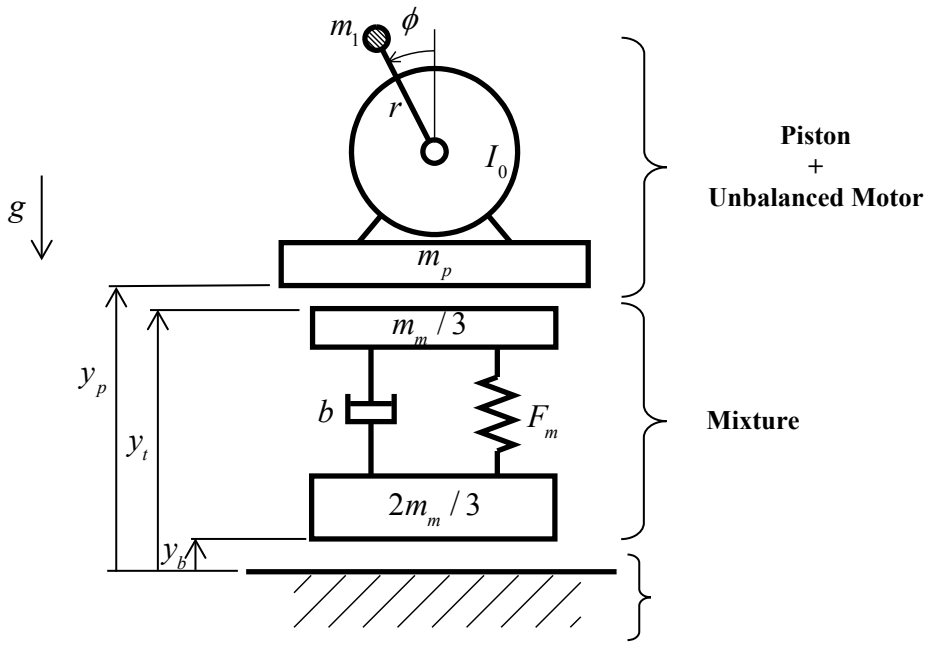

Fig. 5 – 4-DOF model of the vibrocompaction process

Notice that the total mass of the mixture is distributed in the proposed model in a particular way: one third corresponds to the upper mass and two thirds to the bottom mass. This can be justified by recalling a well-known result from vibration theory. Consider an elastic element with uniformly distributed mass which vibrates axially, with one fixed end and a concentrated mass attached to other. Then, if the concentrated mass is substantially greater than the distributed mass, the latter can be replaced, with very good approximation, by an additional concentrated mass at the end, whose value is one third of the total distributed mass [18].

Assuming the mass of the mixture to be uniformly distributed along its thickness, and taking into account that the piston is much heavier than the mixture, the above result is applicable to the vibrocompaction model, as long as there are no separations at any of the contacts.

Rigorously speaking, whenever separation occurred, the deformed shape of the mixture during its vibration would change and, therefore, the distribution of its mass in a couple of equivalent masses should be different. The possibility of modifying this mass distribution depending on the contact status has not been considered in this model in order to keep it as simple as possible, while retaining the essential characteristics of the process. This could be taken as a possible improvement for more sophisticated models which may be built upon the presented one. Nevertheless, it will be seen in Section 3 that, in most cases, the mixture does remain in continuous contact with the piston and the mould during the whole process.

The driving torque provided by the motor minus the losses torque due to friction at the bearings and windage is assumed to be a linear function of the rotor speed:

$$L_m(\dot{\phi}) = A + D\dot{\phi}, \tag{1}$$

with $A > 0$, $D < 0$.

The equations of motion of the system can be obtained by either equilibrium considerations or any other analytical mechanics approach like Lagrange's method or Hamilton's principle:

$$\left\{\begin{array}{c} (m_p + m_1)\ddot{y}_p = m_1 r\left(\dot{\phi}^2 \cos\phi + \ddot{\phi}\sin\phi\right) + F_{ct} - (m_p + m_1)g \\ \frac{m_m}{3}\ddot{y}_t + F_m + b\left(\dot{y}_t - \dot{y}_b\right) = -F_{ct} - \frac{m_m}{3}g \\ \frac{2m_m}{3}\ddot{y}_b - F_m - b\left(\dot{y}_t - \dot{y}_b\right) = F_{cb} - \frac{2m_m}{3}g \\ I\ddot{\phi} = L_m(\dot{\phi}) + m_1 r\sin\phi\left(\ddot{y}_p + g\right) \end{array}\right\}, \tag{2}$$

where $I \equiv I_0 + m_1 r^2$ and F_{cb}, F_{ct} represent the normal contact force between mixture and mould and between mixture and piston, respectively. Details of the contact modelling can be found in Appendix A. Clearly, the most challenging features of this model are the behaviour of the nonlinear spring and the computation of the contact forces. System (2), together with the definition of the spring force and the contact forces given in the following, constitutes the proposed model for the compacting machine.

2.1. Proposed Nonlinear Spring to Model Compaction

The mechanical behaviour of the compacting mixture is extremely complex and necessarily nonlinear, since the mixture suffers irreversible deformation during compaction. An accurate description of this constitutive law would require modelling the motion of the bubbles through the mixture, the friction between quartz particles,

the interaction between quartz and resin, etc. Some investigations about suitable constitutive laws for compacting materials can be found in [19–25].

A simplified constitutive law is proposed in this paper, based on the qualitative observations made on the real material. This phenomenological model intends to capture the two main features of compaction:

1. When a compressive force is applied on the material, it deforms in a nonlinear hardening way. This means that the deforming body stiffens when it becomes more compacted, as a consequence of the increasing packing density of the grains.
2. If the compressive load is released, some of the deformation remains –irreversible deformation due to compaction–, while the rest is recovered –elastic deformation–.

Then, following the two rules above, a nonlinear spring is proposed to model the mixture mechanical behaviour. Fig. 6 represents force F_m produced by the spring against the spring displacement

$$\Delta L \equiv y_t - y_b - L_0, \tag{3}$$

where L_0 is the undeformed length of the spring.

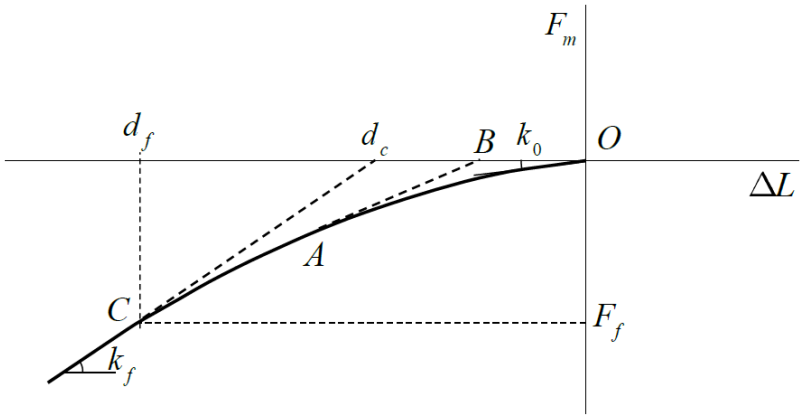

Fig. 6 Force-displacement curve of the nonlinear spring

The behaviour is as follows. Starting from the undeformed position O, a compressive force makes the spring follow a parabolic path of the hardening type, with an initial tangent stiffness k_0. Suppose that, at an intermediate state of compaction A, the force is reversed until reaching an unloaded state. The spring follows the straight line AB, which is tangent to the parabolic curve at point A. Note that, already at this stage, the spring stiffness has increased with respect to the initial value k_0. Note also that, at point B, some plastic deformation remains, corresponding to the level of compaction achieved, while the elastic part of the deformation has been recovered.

If a compressive load is applied again, the material deforms along the elastic path BA, followed by the hardening parabolic line. The complete compaction is defined by point C, where the tangent nonlinear stiffness is k_f. Whenever point C is reached, the mixture becomes totally compacted, and any subsequent loading would only produce elastic deformations with stiffness k_f. Parameter d_c in Fig. 6 represents the irreversible deformation of the mixture when it is unloaded and totally compacted.

The assumption that the elastic return should be tangent to the compaction curve is based on the idea that, once the mixture has achieved certain stiffness by compaction, it keeps the same stiffness during the unloading process. Since the increased stiffness is associated to a more compact packing of the quartz particles, and this new grains distribution does not change during unloading, it seems reasonable to consider that the mixture maintains the reached stiffness level. However, it would be straightforward to modify the model in order to take other types of elastic return into account.

If, at any point of the process, the spring was subjected to a tension load, it would respond linearly and elastically, with the stiffness exhibited by the spring immediately before the tension load was applied. This means that all the linear paths in Fig. 6 –each one with its particular slope– can be extended into the region of positive values of F_m. It should be noted that this scenario is not usual, because the large weight of the piston will make the spring work mainly in compression. However, if separations between mixture and piston occur, some tension forces in the spring can be expected.

More generally, note that the force between the two masses which model the mixture is given by $F_m + b\left(\dot{y}_t - \dot{y}_b\right)$. The fact of this force becoming positive during a particular simulation would imply an internal tension force in the mixture. Observe that this situation –typical during periods of separation at the top and bottom of the mixture– can be physically sound, since the resin provides some adhesion to the mixture, thereby giving it some resistance to tension forces.

The behaviour of the spring is completely defined by specifying F_f, d_f and $R_k \equiv {k_0}/{k_f}$. Below it is shown how to obtain the expression of the parabolic path from these three parameters.

The parabola is given by

$$F_m(\Delta L) = c_1 \Delta L^2 + c_2 \Delta L + c_3, \tag{4}$$

where the three coefficients can be obtained by imposing the following conditions:

$$F_m(0) = 0 \Rightarrow c_3 = 0 \tag{5}$$

$$F_m(d_f) = F_f \Rightarrow F_f = c_1 d_f^2 + c_2 d_f \tag{6}$$

$$\left.\begin{matrix} F_m^{'}(d_f) = k_f \Rightarrow 2c_1 d_f + c_2 = k_f \\ F_m^{'}(0) = k_0 \Rightarrow c_2 = k_0 \end{matrix}\right\} \Rightarrow \frac{1}{R_k} = 1 + \frac{2c_1 d_f}{c_2} \tag{7}$$

By combining (6) and (7), c_1 and c_2 can be calculated:

$$\begin{bmatrix} c_1 \\ c_2 \end{bmatrix} = \begin{bmatrix} d_f^2 & d_f \\ -2d_f & \dfrac{1-R_k}{R_k} \end{bmatrix}^{-1} \begin{bmatrix} F_f \\ 0 \end{bmatrix} \tag{8}$$

Once c_1, c_2 and c_3 are known, the initial and final stiffnesses are obtained as

$$k_0 = c_2,\ k_f = {k_0}/{R_k}\,. \tag{9}$$

Finally, it is useful to characterize the quality of the process for a particular simulation by the level of compaction achieved, defined as

$$\gamma = \frac{k_p - k_0}{k_f - k_0}, \tag{10}$$

where k_p is the stiffness of the spring once the dynamic compaction process has finished. Thus, $\gamma = 0$ corresponds to a totally uncompacted mixture and $\gamma = 1$ represents a case of complete compaction. It is also practical to define a static level of compaction, in order to distinguish how much of the total compaction is due to the weight of the piston and how much is consequence of the vibration process:

$$\gamma_{st} = \frac{k_{st} - k_0}{k_f - k_0}. \tag{11}$$

In equation (11), k_{st} represents the system stiffness after the mixture has been statically compacted by the weight of the masses located above the spring –mainly the weight of the piston–. This initial stiffness can be obtained as

$$k_{st} \equiv \left.\frac{dF_m}{d(\Delta L)}\right]_{\Delta L = d_{st}} = 2c_1 d_{st} + c_2, \tag{12}$$

where, as shown in Fig. 7, d_{st} stands for the lenght variation of the spring due to the weight of the masses above it:

$$d_{st} = \frac{-c_2 + \sqrt{c_2^2 - 4c_1 mg}}{2c_1}. \tag{13}$$

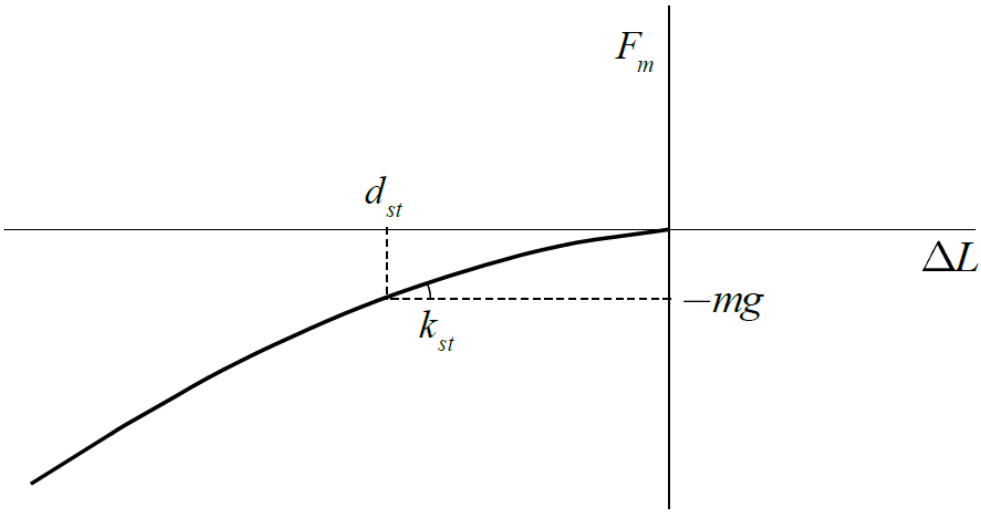

Fig. 7 Graphical definition of parameters d_{st} and k_{st}

Note that the proposed spring model, while being very simple, is able to capture the essential features of compaction, thereby representing a reasonable choice to model the vibrocompaction process. Note that the presented phenomenological model for the mechanical behaviour of the mixture is in qualitative accordance with the results in [23]. Clearly, many other curves could be proposed for the hardening line of the model, instead of a parabola. Some models in the literature use inverse logarithmic [25] or exponential laws [22], as explained in [24]. Then, it would be desirable, as a further step in the investigation of compaction processes, to compare experimental results with different hardening laws (parabolic, cubic, exponential,…) in order to see what expression provides a better fitting. A discussion on the energy flow in the model can be found in Appendix B.

3. Numerical Simulations

General Description of the Simulations

In this section, system (2) is numerically solved for different scenarios. The chosen initial conditions for all the simulations correspond to the static equilibrium position of the system (see Fig. 8):

$$\left\{\begin{array}{c}\phi(0)=\pi\\ \dot{\phi}(0)=0\\ y_b(0)=d_b\\ \dot{y}_b(0)=0\\ y_t(0)=d_b+L_0+d_{st}\\ \dot{y}_t(0)=0\\ y_p(0)=d_b+L_0+d_{st}+d_t\\ \dot{y}_p(0)=0\end{array}\right\}, \tag{14}$$

where d_t and d_b are the indentations at the top and bottom contacts, respectively, due to the weight of the elements above the contact:

$$d_t=\frac{-(m_p+m_1)g}{k_c},\ d_b=\frac{-(m_p+m_1+m_m)g}{k_c}. \tag{15}$$

With this initial configuration, system (2) is solved, using embedded Runge-Kutta formulae of orders 4 and 5, for a simulation time t_f which varies between $30s$ and $55s$. This total time includes three different stages in the simulation, of respective lengths t_1, t_2 and t_3 $(t_f=t_1+t_2+t_3)$:

3. During the first stage $(0\le t<t_1)$ parameter A is linearly increased from A_0 to A_f, with A_0 and A_f being defined for each particular simulation. The slope D is kept constant along the process, which implies that the motor characteristics is displaced parallel to itself. Then, at this stage, the motor is being controlled as in Sommerfeld's experiment explained in Fig. 3.
4. At the second stage $(t_1\le t<t_1+t_2)$, parameter A is kept constant at its final value A_f. During this stage, the machine is expected to reach a stationary operating point.
5. At time $t=t_1+t_2$, the motor is switched off in order to let the system reach a compacted equilibrium position. Clearly, once the motor is switched off, there is no driving torque on the rotor, and function $L_m(\dot{\phi})$ must only account for the resisting torque due to windage and friction at the bearings. This is modelled by replacing the motor characteristic with the following curve:

$$L_m(\dot{\phi})=0.2\cdot D\dot{\phi},\ \text{for}\ t_1+t_2\le t<t_f. \tag{16}$$

Hence it is being assumed that the slope of the resisting torque curve is 20% of the slope of the motor characteristic.

Parameters t_2 and t_3 have been chosen as $15s$ for all the simulations, while t_1 will take different values depending on the case under study.

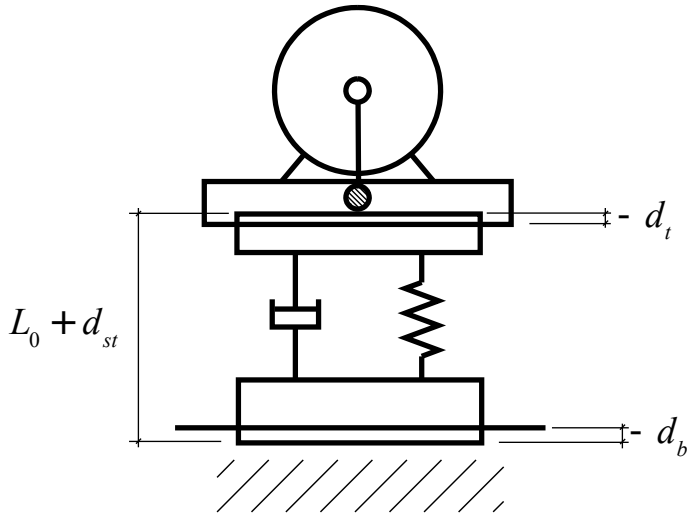

Fig. 8 Initial configuration of the system, with the contact indentations exaggerated for clarity.

Case 1 (Reference)

The proposed model (2) is defined by 11 dimensional parameters

$$\{m_1, m_p, m_m, b, r, I_0, d_f, F_f, R_k, k_c, b_c\}, \tag{17}$$

besides the two parameters associated to the motor control

$$\{A, D\}. \tag{18}$$

For this first simulation, the set of parameters (17) is chosen as

$$\left\{\begin{array}{c} m_1 = 20\text{kg},\ m_m = 240\text{kg},\ m_p = 1.5 \cdot 10^3\text{kg} \\ r = 0.1\text{m},\ I_0 = 0.84\text{kgm}^2,\ b = 4 \cdot 10^3\text{Ns/m} \\ d_f = -0.1\text{m},\ F_f = -1 \cdot 10^5\text{N},\ R_k = 0.1 \\ k_c = 3 \cdot 10^9\text{N/m},\ b_c = 9.5 \cdot 10^6\text{Ns/m} \end{array}\right\}. \tag{19}$$

Before the numerical resolution of the equations of motion, it is useful to obtain some previous information about the system. First, from the knowledge of parameters $\{d_f, F_f,\ R_k\}$, stiffnesses k_0 and k_f can be computed through relations (8) and (9):

$$k_0 = 1.82 \cdot 10^5 \mathrm{N/m},\ k_f = 1.82 \cdot 10^6 \mathrm{N/m} \tag{20}$$

Using (12) and (13), the initial stiffness for the dynamic process can also be obtained, together with the static compaction:

$$k_{st} = 7.39 \cdot 10^5 \mathrm{N/m} \Rightarrow \gamma_{st} = 34.1\%. \tag{21}$$

A numerical experiment is carried out now, where the motor control parameters are chosen as

$$t_1 = 10\mathrm{s},\ D = -5\mathrm{Nms},\ \mathrm{A}_0 = 20\mathrm{Nm},\ \mathrm{A}_f = 140\mathrm{Nm}. \tag{22}$$

The corresponding torque-speed curves are represented in Fig. 9, where notation

$$L_{m0} = \mathrm{A}_0 + D\dot{\phi},\ L_{mf} = \mathrm{A}_f + D\dot{\phi} \tag{23}$$

has been used. The results of the simulation are represented in Fig. 10 and Fig. 11.

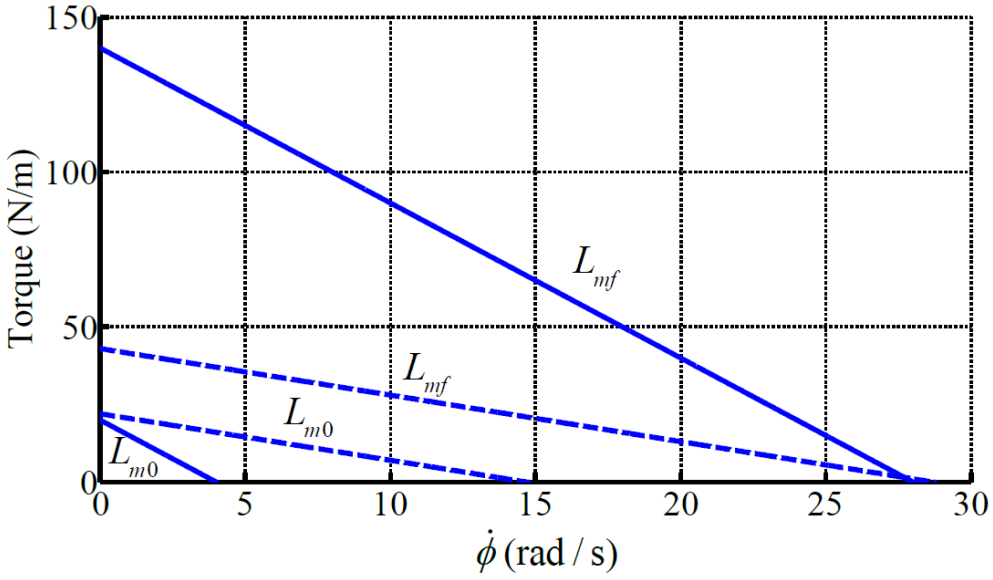

Fig. 9 Motor characteristics for Case 1 (solid line) and Case 2 (dashed line)

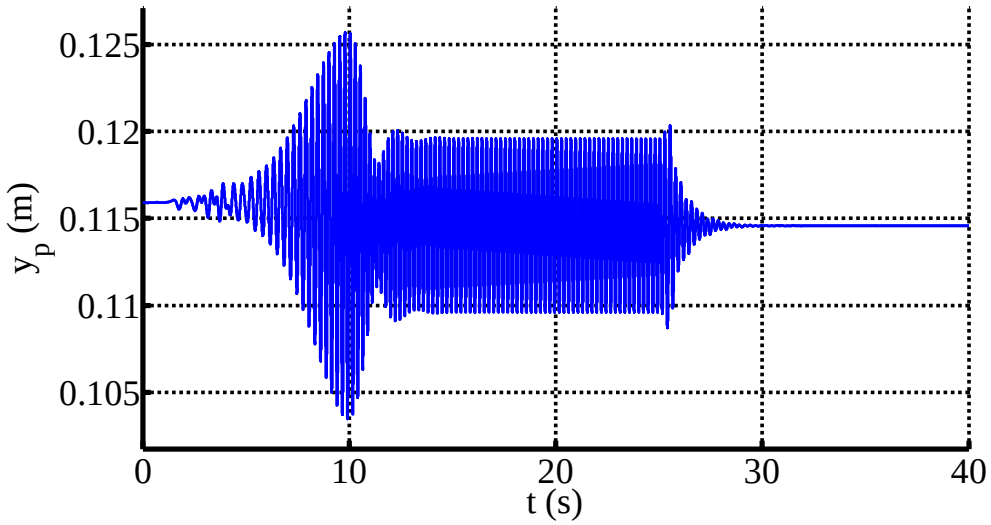

Fig. 10 Piston displacement for Case 1

It is observed in Fig. 10 that, as the motor curve is displaced upwards between 0 and 10s, the oscillation amplitude grows monotonically, until a point where a jump phenomenon is encountered. After the jump, the system clearly reaches a post resonant state of motion, as shown in Fig. 11, where ω_{np} represents the natural frequency of the system during the stationary motion of stage 2. This value is obtained as

$$\omega_{np} = \sqrt{\frac{k_p}{m_p + m_m/3 + m_1}}, \tag{24}$$

where k_p denotes the stiffness exhibited by the nonlinear spring during the attained stationary motion $(k_0 < k_p \leq k_f)$.

The jump phenomenon encountered here clearly resembles the Sommerfeld effect described in the introduction. However, it seems to be somehow different to the general phenomenon shown in Fig. 2, since no clear slowing down in the increase of the rotor speed is observed in Fig. 11.

As was explained in the introduction, the Sommerfeld effect in the simple system depicted in Fig. 1 can be readily explained by using a torque-speed graph, such as that shown in Fig. 3. The idea is that the possible stationary motions of the system can obtained as the intersections between two torque-speed curves, corresponding to the driving torque produced by the motor and the resisting torque due to vibration, respectively.

It is reasonable to expect that the same kind of torque-speed plot can also be obtained for the vibrocompaction model under investigation, which would shed light on the particular way in which the Sommerfeld effect is present in the system. This can actually be done but, due to the increased complexity of the model –nonlinear spring allowing for permanent deformations and possibility of separations and impacts–, the analytical approach needed to obtain the curves is not straightforward. In particular, note that the stiffness of the vibrating system under study is not fixed, but can take different values from k_0 to k_f. This implies that, instead of having one vibration torque curve, there will be a family of curves, one for each possible value of the spring stiffness. Then,

some detailed explanations are necessary to justify the computation and interpretation of the torque-speed curves, which would make the present paper much too long. For this reason, the authors intend to present these additional results in a subsequent paper.

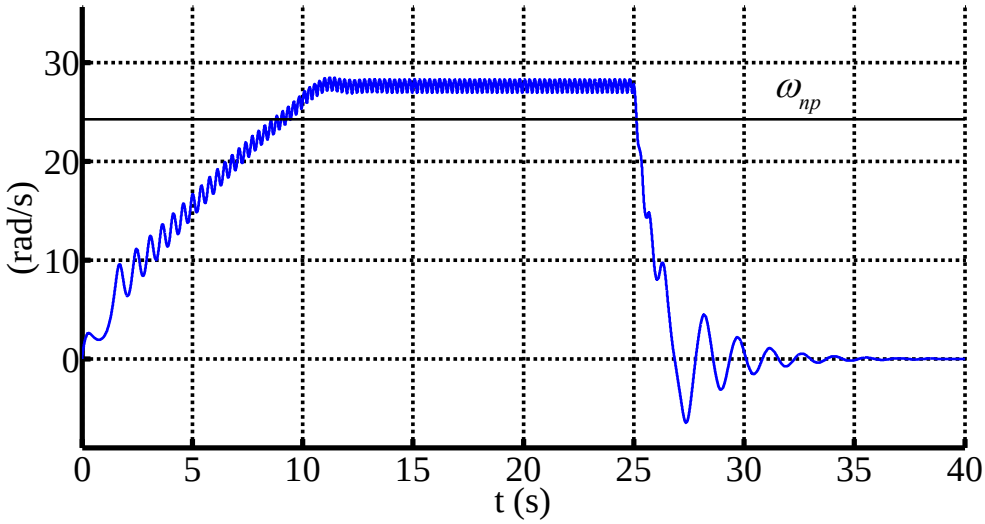

Fig. 11 Rotor speed for Case 1

Note the difference between the initial and final position of the piston in Fig. 10, which reveals the compaction due to vibration. Regarding the top and bottom contacts, no separations or impacts were found in this case. Hence the displacements of the mixture, which do not give much significant information, have not been represented.

Finally, the level of compaction achieved can be obtained through relation (10):

$$\gamma = 46.5\%. \tag{25}$$

Case 2 (Different Motor Curves)

In this second simulation, the set of parameters (19) is maintained, while the parameters related to the motor control are now set to

$$t_1 = 15\text{s},\ D = -1.5\text{Nms},\ \mathrm{A}_0 = 22\text{Nm},\ \mathrm{A}_f = 43\text{Nm}. \tag{26}$$

The torque-speed curves corresponding to this new control of the motor are represented in Fig. 9, where they can be directly compared to those in Case 1. The numerical results obtained for this scenario are shown in Fig. 12 and Fig. 13. No separations or impacts were observed.

Note that no jump phenomenon takes place in this case: the vibrating amplitude grows until reaching a stationary state, where the average rotor speed is slightly below the resonance frequency ω_{np} (see Fig. 13). Then, it is apparent that the motor torque is not large enough in this case to make the system jump through resonance.

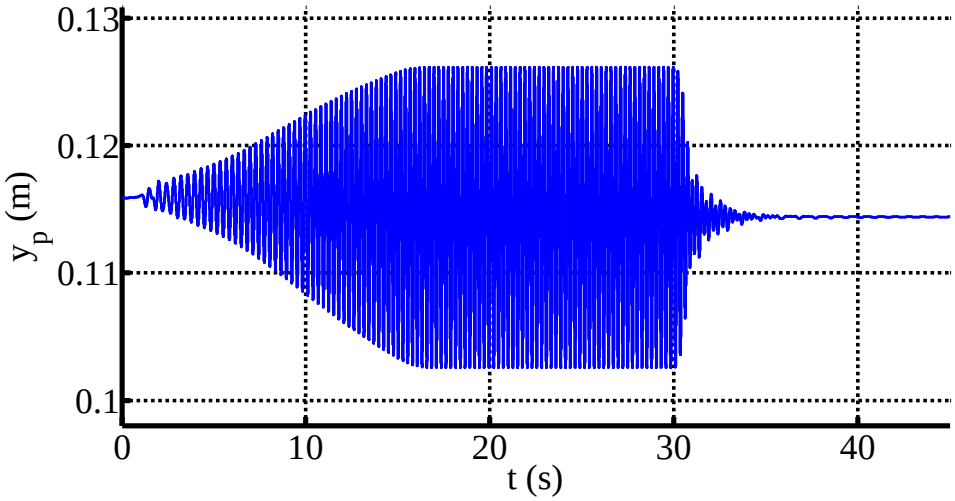

Fig. 12 Piston displacement for Case 2

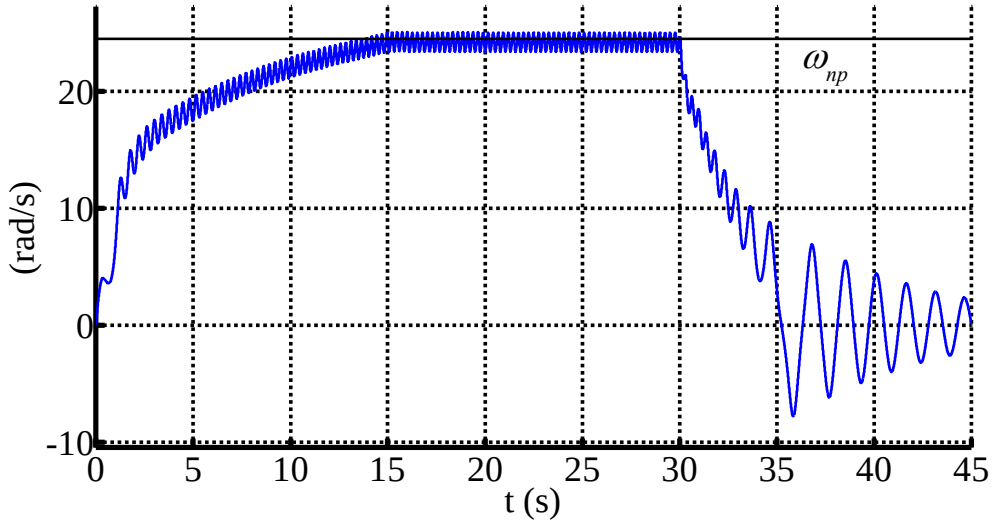

Fig. 13 Rotor speed for Case 2

The level of compaction attained in this simulation is lightly greater than in Case 1:

$$\gamma = 47.4\%. \tag{27}$$

It is evident that the motor control parameters $\{A,D\}$ have a major influence on the compacting machine behavior. They define the maximum amount of power that the motor can develop and may affect the stationary regime of motion attained by the system, as observed by comparing the results of Cases 1 and 2.

Following the comments on the Sommerfeld effect made in the discussion of Case1, it is clear that plotting a torque-speed graph for the vibrocompaction system would be especially useful to better understand the effect of the motor characteristic on the system dynamics. This representation would allow predicting how the possible regimes of motion of the machine are affected by changes in the motor characteristic. As was justified before, the analytical approach which leads to the torque-speed representation is left for a second paper because of space constraints.

Case 3 (No Motor Control)

This case is intended to investigate the effects of transient motions in the dynamics of compaction. Thus, in the present scenario, the motor is not controlled in such a way that its torque curve is slowly displaced, as in previous cases. Instead, the motor characteristic is now set to its final position from the beginning of the process.
All the parameters in the simulation are like in Case 2, except for the time associated to the first stage, which is now set to

$$t_1 = 0\text{s}. \tag{28}$$

This is equivalent to say that there is no motor control. The results of this simulation are shown in Fig. 14 and Fig. 15, where an utterly different behavior to that of Case 2 is found.

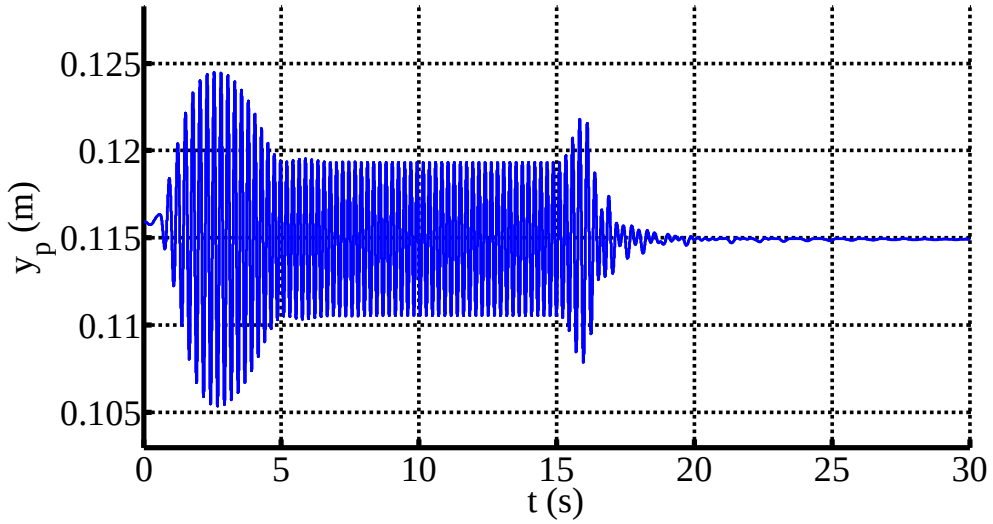

Fig. 14 Piston displacement for Case 3

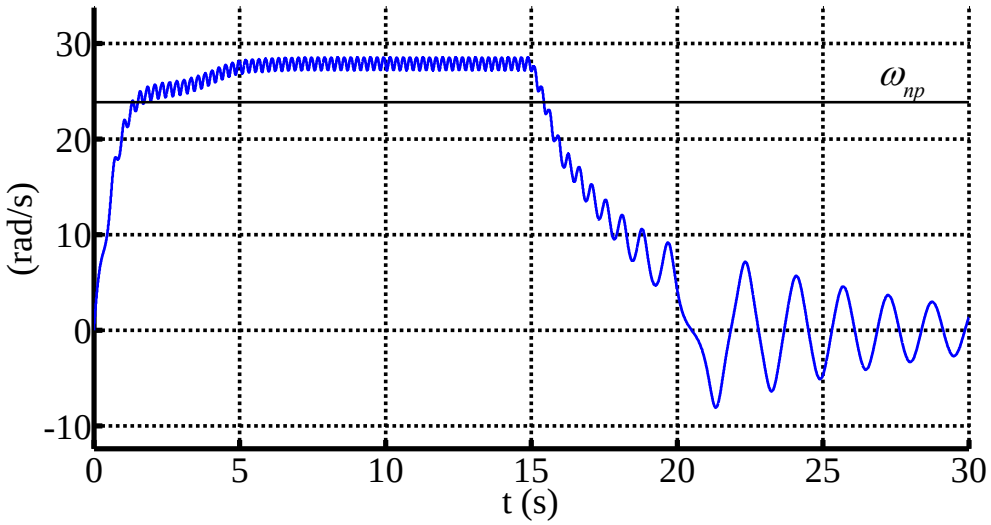

Fig. 15 Rotor speed for Case 3

Noticeable, the jump phenomenon typical from nonideal excitations, is indeed observed here, while it was not in Case 2. Since the only difference between these two simulations is parameter t_1, it is clear that the jump encountered in Fig. 14 and Fig. 15 is produced by the transient effects associated to the absence of a motor control. In Cases 1 and 2, the system is made to evolve from one operating point to another by gradually displacing the motor curve. Conversely, in the present case, the motor curve is fixed from the beginning, and the system evolves according to equations (2) until reaching a stationary state. It is observed that this transient behavior makes the system jump through resonance (see Fig. 15).

Interestingly, a less compacted mixture is obtained in this simulation than in Case 2:

$$\gamma = 44.6\%. \tag{29}$$

This is a physically sound result because, due to the jump to a post-resonant regime, the vibration amplitude reached in Case 3 is smaller than in Case 2. Clearly, according to the spring model proposed in Section 2.1, the larger the amplitude of the mixture vibration, the more compacted it becomes. From the comparison between Cases 2 and 3, it is evident that a deep knowledge and control of the jump phenomenon would be extremely useful in order to achieve an optimal compaction.

Case 4 (No Motor Control, Increased Rotor Inertia)

This new scenario is identical to *Case 3*, with the exception of a greater rotor inertia, which takes three times the previous value:

$$I_0 = 2.52\text{kgm}^2. \tag{30}$$

Then, the comparison between Cases 3 and 4 will serve as an illustration of the kind of effect that the rotor inertia can have on the machine behaviour. Like in Case 3, no motor control is considered here. Instead, the motor characteristic is fixed at its final position from the beginning of the process.

The results of this simulation, represented in Fig. 16 and Fig. 17, display a significant feature: the jump through resonance, which occurred in Case 3 –see Fig. 14 and Fig. 15–, does not take place here. The rotor speed stabilizes slightly below the resonance frequency ω_{np} and, consequently, the system vibrates with larger amplitude than in Case 3. Like in previous cases, no separations were found between the contacting surfaces.

Interestingly, it can also be observed, by comparing Fig. 16 and Fig. 17 to Fig. 12 and Fig. 13, that the results obtained in this case are very similar to those corresponding to Case 2. In fact, the final level of compaction in the present simulation turns out to be

$$\gamma = 47.4\%, \tag{31}$$

which totally coincides with the compaction achieved in Case 2 –see (27)–.

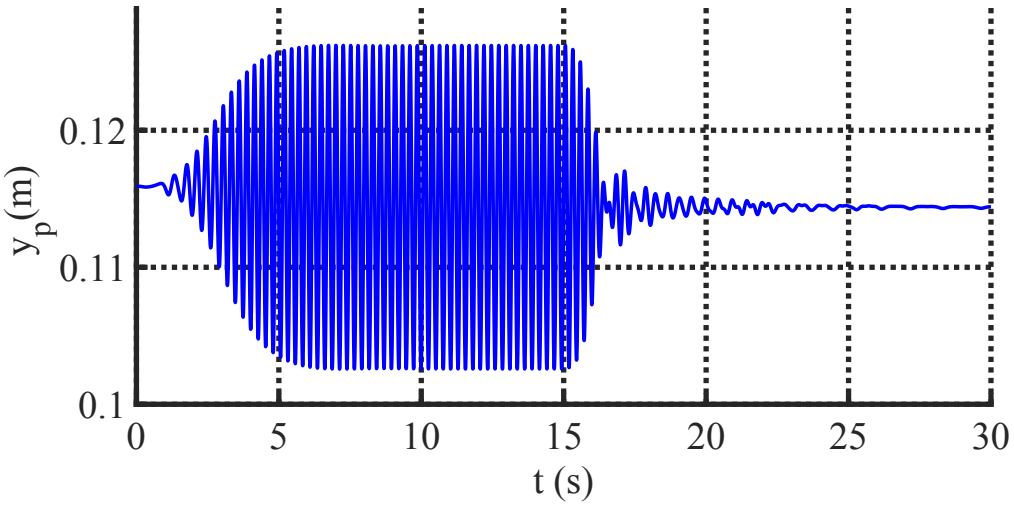

Fig. 16 Piston displacement for Case 4

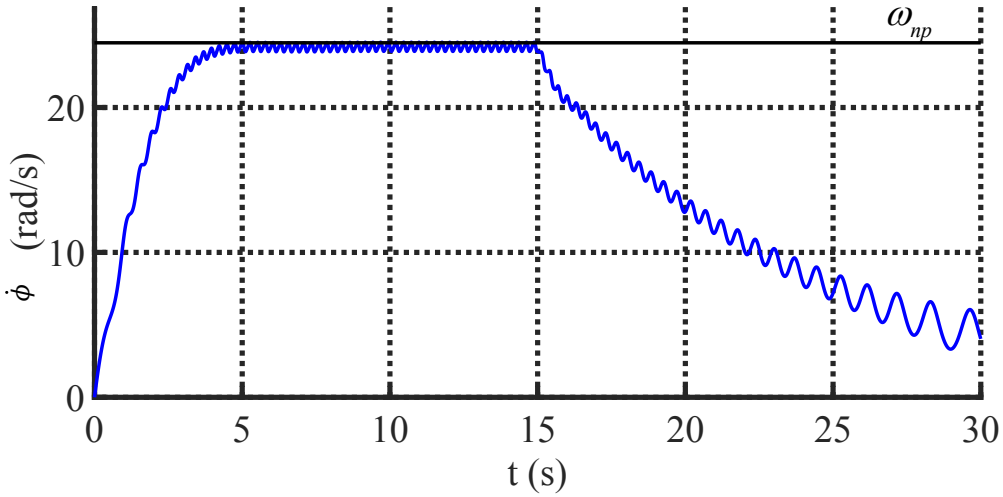

Fig. 17 Rotor speed for Case 4

This similarity is relevant because it gives some insight into the influence of the rotor inertia on the machine dynamics. Recall that, in Case 2, the motor characteristic was slowly displaced upwards during the first stage of the simulation $(0 \leq t < t_1)$, corresponding to an increase in the motor input power, until reaching a stationary regime of motion during the second stage $(t_1 \leq t < t_2)$. This corresponded to a near-resonant vibration, as depicted in Fig. 12 and Fig. 13. In Case 3, the time length associated to the first simulation stage was reduced to 0, meaning the elimination of the motor control. It was shown that the transient effects produced by this lack of control made the system jump to a post-resonant vibration (Fig. 14 and Fig. 15), whose smaller amplitude produced a less effective compaction of the mixture. Noticeably, the increase in the rotor inertia considered in Case 4, while maintaining $t_1 = 0$, eliminates the jump phenomenon and yields the kind of behaviour obtained when the motor input power was gradually increased.

This is physically intuitive: a larger rotor inertia reduces the angular accelerations of the rotor, making the rotor speed evolve in a gentler manner. The greater the inertia, the slower the increase of the rotor speed during its raise from zero to its stationary value. Then, the effect of a large inertia is similar to continuously displacing the motor characteristic in order to have a controlled evolution of the rotor speed. In other words, a greater rotor inertia mitigates the transient effects associated to an absence of motor control and can influence the appearance of Sommerfeld's jump phenomenon.

Case 5 (Unbalanced Mass Doubled)

The fifth case under study maintains all parameters (19) of Cases 1-3, except for the unbalanced mass, which is now doubled:

$$m_1 = 40\text{kg}. \tag{32}$$

This is a clear example of how the presented model can be used to analyze the influence of certain system parameters on the final result of the process. In this case, it is rather intuitive that a larger unbalanced mass will enhance the vibrocompaction process, since larger centrifugal forces in the motor will be generated.

While parameters k_0 and k_f are the same as in Case 1, there is some variation in the initial stiffness and compaction, due to the increased weight of the system:

$$k_{st} = 7.44 \cdot 10^{5}\mathrm{N/m} \Rightarrow \gamma_{st} = 34.3\%. \tag{33}$$

The equations of motion (2) are numerically solved for the following motor control:

$$t_1 = 15\mathrm{s},\ D = -2.3\mathrm{Nms},\ \mathrm{A}_0 = 40\mathrm{Nm},\ \mathrm{A}_f = 80\mathrm{Nm}, \tag{34}$$

and the obtained results are represented in Fig. 15-Fig. 21. No jump phenomenon was observed in this case.

The first apparent difference between this case and the preceding ones is that separations are observed here between piston and mixture, and also between mixture and mould. This is evidenced by the displacements in Fig. 18 and Fig. 19 –recall that a positive value for y_b represents separation between the mixture and the mould– and also by the contact forces in Fig. 21. During a time interval which roughly corresponds to $11\mathrm{s} < t < 30\mathrm{s}$, the contact forces become zero for certain periods, followed by an abrupt increase in the force associated to the impact between the contacting bodies. In particular, note that the impacts between the piston and the mixture produce peaks in the contact force which are around ten times the weight of the piston. Note also the complex time evolution of the forces in the close-up of Fig. 21(b).

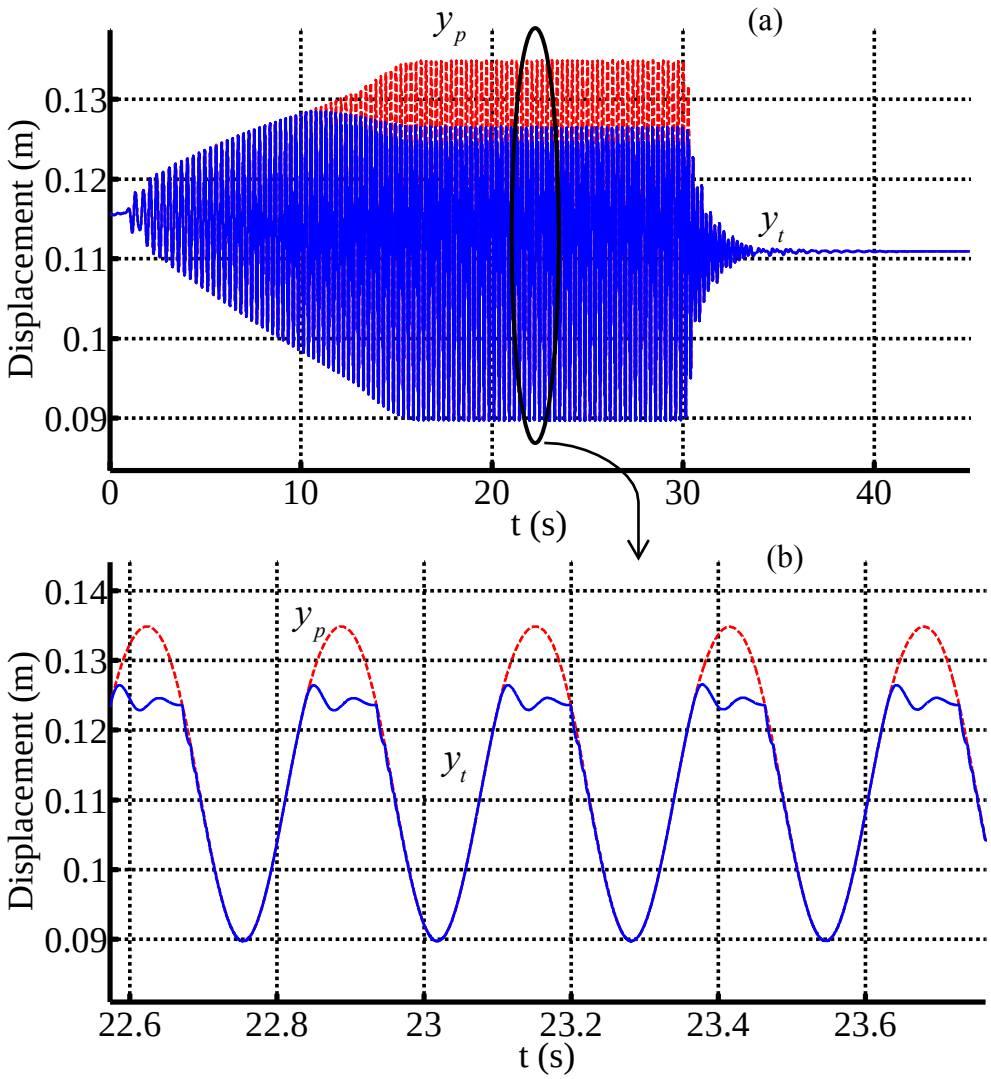

Fig. 18 Displacements of the piston and the top of the mixture for Case 5. The red line corresponds to the position of the piston, y_p, while the blue line corresponds to the position of the top of the mixture, y_t.

(a) Full view

(b) Close-up

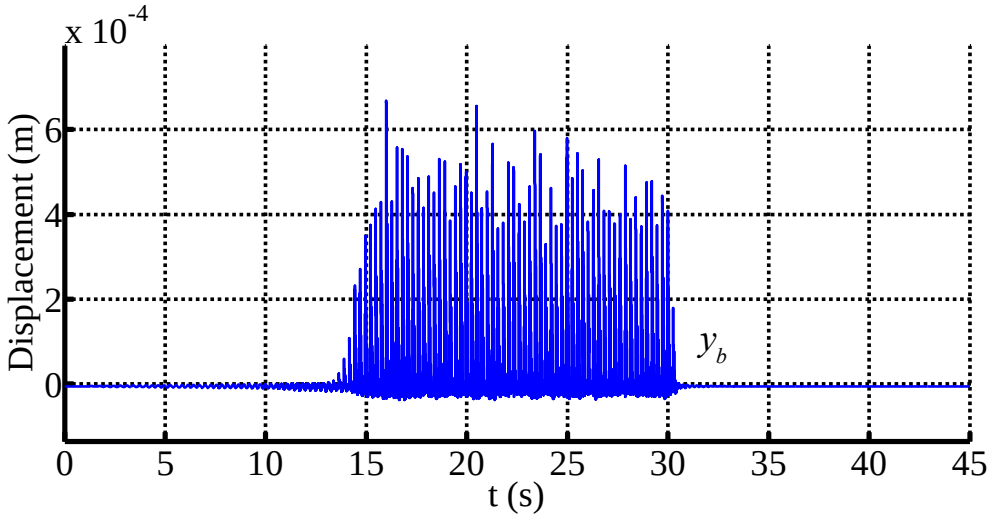

Fig. 19 Displacement of the bottom of the mixture for Case 5

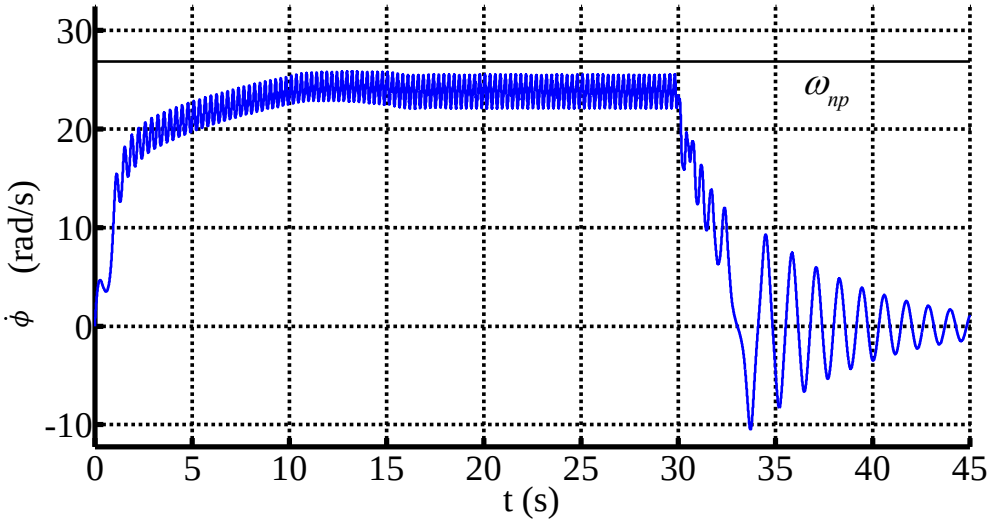

Fig. 20 Rotor speed for Case 5

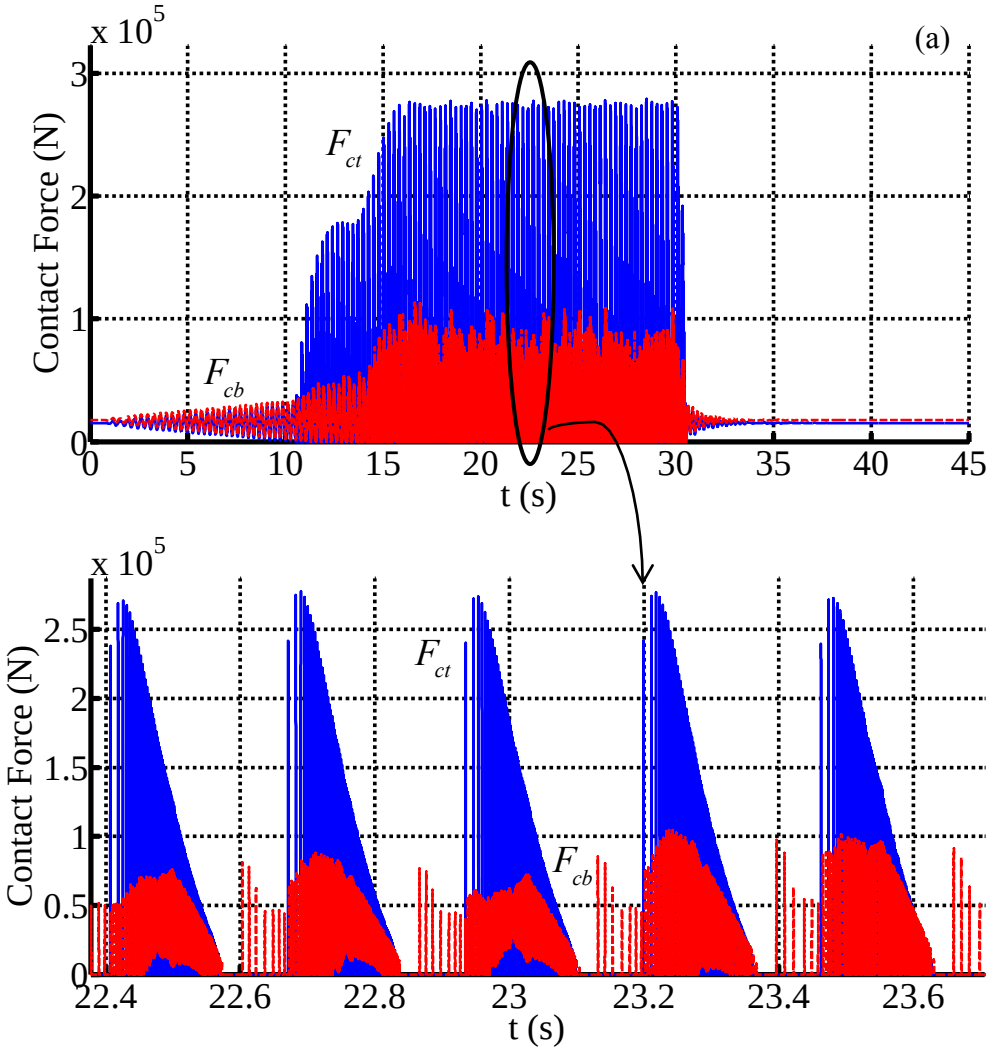

Fig. 21 Contact forces for Case 5. The red line corresponds to the normal contact force between mixture and mould, F_{cb}, while the blue line corresponds to the normal contact force between mixture and piston, F_{ct}.

(a) Full view

(b) Close-up

This simulation produces a final compaction of

$$\gamma = 60.3\%, \tag{35}$$

which is greater than in all previous cases. This is in accordance with the physical intuition that a greater unbalanced mass produces larger exciting forces, thereby giving rise to a more effective compaction.

Case 6 (Piston Mass Doubled)

Finally, it is also illustrative to analyse the effect of the piston mass on the result of the process. To this end, the set of parameters (19) of Case 1 is maintained, except for the mass of the piston, which is doubled:

$$m_p = 3 \cdot 10^3 kg. \tag{36}$$

It is relevant to note that the effect of such a modification is in principle not obvious. Clearly, a heavier piston will increase the static compaction of the mixture γ_{st}. However, the unbalanced mass becomes relatively less significant, with respect to the total mass of the system, which may produce a less effective dynamic compaction.

Note that, since the constitutive law of the nonlinear spring has not been modified, stiffnesses k_0 and k_f are the same as in Case 1. On the contrary, as commented above, the proposed modification will increase the static compaction due to the weight of the piston. Relations (12) and (13) yield

$$k_{st} = 1.01 \cdot 10^6 \mathrm{N/m} \Rightarrow \gamma_{st} = 50.9\%. \tag{37}$$

The motor control parameters chosen for the simulations are

$$t_1 = 25\mathrm{s},\ D = -1.5\mathrm{Nms},\ \mathrm{A}_0 = 22\mathrm{Nm},\ \mathrm{A}_f = 34\mathrm{Nm}, \tag{38}$$

which produces the results depicted in Fig. 22 and Fig. 23.

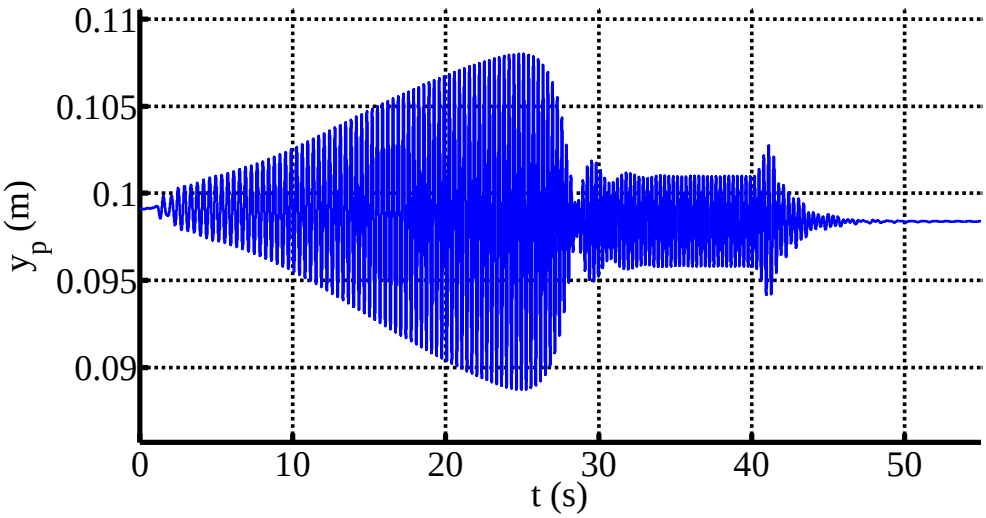

Fig. 22 Piston displacement for Case 6

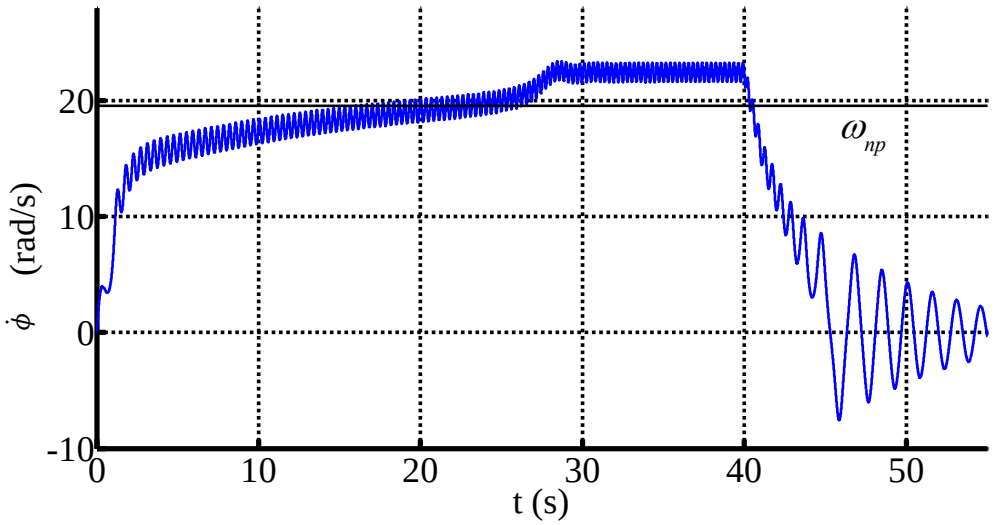

Fig. 23 Rotor speed for Case 6

No separations were found at any of the contacts in this scenario. This was very much expected, since the increased weight of the piston produces greater contact forces. The system clearly exhibits a jump phenomenon towards a post-resonant operating point. The final level of compaction achieved is

$$\gamma = 61.2\%, \tag{39}$$

which is larger than in all previous cases. Then, it is found that the beneficial static effect of a heavier piston is in this case dominant against the detrimental dynamic effect of a smaller relative unbalanced mass. Observe, by comparing (37) and (39), that only a small fraction of this total compaction is due to the dynamic process.

This simulation shows that the proposed model can be used to evaluate how certain parameter modifications will affect the result of the process, especially in situations where such an evaluation is not clear from physical intuition.

The results of all the conducted simulations are summarized in Table 1.

Table 1 Summary of results for the conducted simulations

Considered Scenario	**Static Compaction γ_{st}**	**Total Compaction γ**
Case 1	34.1%	46.5%
Case 2	34.1%	47.4%
Case 3	34.1%	44.6%
Case 4	34.1%	47.4%

Case 5	34.3%	60.3%
Case 6	50.9%	61.2%

Finally, it should be noted that the different simulations considered in this section do not intend to constitute a comprehensive study of the effect of each parameter on the mixture compaction (a systematic investigation with much more combinations of parameters would be necessary for this purpose). Rather, they should be seen as illustrative examples of the kind of predictions and analysis that the proposed model allows for.

4. Conclusions and Future Work

The most significant contributions of this paper are enumerated as follows:

1. A new nonlinear four degree-of-freedom model has been proposed for the vibrocompaction of quartz agglomerates –which could be easily generalized to other vibrocompaction systems–. The model includes the possibility of separations and contacts/impacts between the compacting mixture and the piston, and also between the mixture and the mould.
2. In addition, a nonlinear spring is used to model the mechanical behaviour of the mixture that is compacted, with a phenomenological constitutive law which includes hardening and permanent deformations due to compaction.
3. The equations of motion of the four degree-of-freedom model have been numerically solved. The results of several case studies differing in the combination of design parameters selected show jump phenomena near resonance, similar to those usually reported in the literature as *The Sommerfeld Effect*.
4. It has been shown that this jump towards a post-resonant regime can be produced by transient motions of the machine. Since the jump phenomenon leads to small-amplitude oscillations, it can be detrimental for the purpose of dynamic compaction.
5. It has also been shown how the presented model can be used to investigate the influence of different parameters of the industrial process in the final result of the compaction. In particular, in the simulations carried out, the process has been found to be enhanced by increasing the piston mass and the amount of unbalance.

Relevant next steps in this research are:

1. Experimental validation of the proposed nonlinear constitutive law for the compacting mixture, and comparison with other proposals in the literature.
2. Analytical investigation on the behaviour of the proposed model, with the purpose of explaining the particular way in which the Sommerfeld Effect is present in the machine, predicting the existence of jump phenomena and controlling their appearance.

Acknowledgements This work was supported by Grant FPU12/00537 of the Spanish Ministry of Education, Culture and Sport. The authors gratefully acknowledge fruitful discussions with Prof. José María Goicolea about

nonlinear constitutive laws for compacting materials. It is also very much appreciated the advice of Prof. Werner Schiehlen to improve the thesis manuscript which gave rise to this paper.

References

[1] V.O. Kononenko, Vibrating Systems with a limited power supply, Illife, London, 1969.
[2] I.I. Blekhman, Vibrational Mechanics-Nonlinear Dynamic Effects, General Approach, Singapore, 2000.
[3] M.F. Dimentberg, L. Mcgovern, R.L. Norton, J. Chapdelaine, R. Harrison, Dynamics of an Unbalanced Shaft Interacting with a Limited Power Supply, Nonlinear Dyn. (1997) 171–187. doi:10.1023/a:1008205012232.
[4] J. González-Carbajal, J. Domínguez, Limit cycles in nonlinear vibrating systems excited by a nonideal energy source with a large slope characteristic, Nonlinear Dyn. (2016). doi:10.1007/s11071-016-3120-7.
[5] J.M. Balthazar, D.T. Mook, H.I. Weber, B. R., A. Fenili, D. Belato, J.L.P. Felix, An Overview on Non-Ideal Vibrations, Meccanica. 38 (2003) 613–621.
[6] J.L.P. Felix, J.M. Balthazar, M.J.H. Dantas, On energy pumping, synchronization and beat phenomenon in a nonideal structure coupled to an essentially nonlinear oscillator, Nonlinear Dyn. 56 (2009) 1–11. doi:10.1007/s11071-008-9374-y.
[7] D.T. Bolla, M. R., Balthazar, J. M., Felix, J. L. P., Mook, On an approximate analytical solution to a nonlinear vibrating problem , excited by a nonideal motor, Nonlinear Dyn. (2007) 841–847. doi:10.1007/s11071-007-9232-3.
[8] L. Munteanu, C. Brişan, V. Chiroiu, D. Dumitriu, R. Ioan, Chaos–hyperchaos transition in a class of models governed by Sommerfeld effect, Nonlinear Dyn. 78 (2014) 1877–1889. doi:10.1007/s11071-014-1575-y.
[9] A.A. El-Badawy, Behavioral Investigation of a Nonlinear Nonideal Vibrating System, J. Vib. Control. 13 (2007) 203–217. doi:10.1177/1077546307073674.
[10] J.L.P. Felix, J.M. Balthazar, Comments on a nonlinear and nonideal electromechanical damping vibration absorber, Sommerfeld effect and energy transfer, Nonlinear Dyn. 55 (2009) 1–11. doi:10.1007/s11071-008-9340-8.
[11] A. Sommerfeld, Naturwissenchftliche Ergebnisse der Neuren Technischen Mechanik, Verein Dtsch. Ing. Zeitscchrift. 18 (1904) 631–636. doi:10.1109/COC.2000.873973.
[12] A.H. Nayfeh, D.T. Mook, Nonlinear Oscillations, John Wiley and Sons, 1995.
[13] J.A. Sanders, F. Verhulst, J. Murdock, Averaging Methods in Nonlinear Dynamical Systems, Springer, New York, 2007.
[14] J. Holtz, I. Paper, J. Holtz, Sensorless control of induction motor drives, Proc. IEEE. 90 (2002) 1359–1394. doi:10.1109/JPROC.2002.800726.
[15] J. González-Carbajal, J. Domínguez, Nonlinear Vibrating Systems Excited by a Nonideal Energy Source with a Large Slope Characteristic, Mech. Syst. Signal Process. (2017).
[16] R.H. Rand, R.J. Kinsey., D.L. Mingori, Dynamics of spinup through resonance, Int. J. Non. Linear. Mech. 27 (1992) 489–502. doi:10.1016/0020-7462(92)90015-Y.
[17] R.J. Kinsey, D.L. Mingori, R.H. Rand, Nonlinear Controller to Reduce Resonance Effects during Despin of a Dual-Spin Spacecraft through Precession Phase Lock, Proc. 31st Conf. Decis. Control. (1992).
[18] L. Meirovitch, Analytical Methds in Vibrations, Macmillan, New York, 1967.
[19] S. Pietruszczak, G.N. Pande, Constitutive Relations for Partially Saturated Soils Containing Gas Inclusions, J. Geotech. Eng. 122 (1996) 50–59. doi:10.1061/(ASCE)0733-9410(1996)122:1(50).
[20] E.E. Alonso, A. Gens, A. Josa, A constitutive model for partially saturated soils, Géotechnique. 40 (1990) 405–430. doi:10.1680/geot.1990.40.3.405.
[21] J.J. Stickel, R.L. Powell, Fluid Mechanics and Rheology of Dense Suspensions, Annu. Rev. Fluid Mech. 37 (2005) 129–149. doi:10.1146/annurev.fluid.36.050802.122132.
[22] P. Richard, M. Nicodemi, R. Delannay, P. Ribiere, D. Bideau, Slow relaxation and compaction of granular systems, Nat Mater. 4 (2005) 121–128.
[23] N. Favrie, S. Gavrilyuk, Dynamic compaction of granular materials, Proc. R. Soc. A Math. Phys. Eng. Sci. 469 (2013).

[24] Kiesgen de Richter, S., Hanotin, C., Marchal, P., Leclerc, S., Demeurie, F., Louvet, N., Vibration-induced compaction of granular suspensions, Eur. Phys. J. E. 38 (2015) 74. doi:10.1140/epje/i2015-15074-7.
[25] J.B. Knight, C.G. Fandrich, C.N. Lau, H.M. Jaeger, S.R. Nagel, Density relaxation in a vibrated granular material, Phys. Rev. E. 51 (1995) 3957–3963. doi:10.1103/PhysRevE.51.3957.
[26] G. Gilardi, I. Sharf, Literature survey of contact dynamics modelling, Mech. Mach. Theory. 37 (2002) 1213–1239. doi:10.1016/S0094-114X(02)00045-9.
[27] K.H. Hunt, F.R.E. Crossley, Coefficient of Restitution Interpreted as Damping in Vibroimpact, J. Appl. Mech. 42 (1975) 440. doi:10.1115/1.3423596.
[28] O. Ma, Contact dynamics modelling for the simulation of the Space Station manipulators handling payloads, in: Proc. 1995 IEEE Int. Conf. Robot. Autom., IEEE, 1995: pp. 1252–1258. doi:10.1109/ROBOT.1995.525453.
[29] M.K. Vukobratović, V. Potkonjak, Dynamics of contact tasks in robotics. Part I: general model of robot interacting with environment, Mech. Mach. Theory. 34 (1999) 923–942. doi:10.1016/S0094-114X(97)00091-8.
[30] A. Haddadi, K. Hashtrudi-Zaad, A new method for online parameter estimation of Hunt-Crossley environment dynamic models, in: 2008 IEEE/RSJ Int. Conf. Intell. Robot. Syst., IEEE, 2008: pp. 981–986. doi:10.1109/IROS.2008.4650575.
[31] S. Bhasin, K. Dupree, P.M. Patre, W.E. Dixon, Neural Network Control of a Robot Interacting With an Uncertain Hunt-Crossley Viscoelastic Environment, in: ASME 2008 Dyn. Syst. Control Conf. Parts A B, ASME, 2008: pp. 875–882. doi:10.1115/DSCC2008-2222.

Appendix A: ***Contact Modelling***

Consider now the contacts present in the model: mixture-mould and mixture-piston. Many different ways of modelling contact have been proposed in the literature over the years –a good overview of the state of the art is given in [26]–. For the present study, a Hunt and Crossley model has been chosen [27]:

$$F_c = k_c\delta^n + b_c\delta^p\dot{\delta}^q, \tag{40}$$

where F_c is the normal contact force, δ is the indentation between the bodies –which represents the local deformation produced by the contact– and k_c, b_c, n, p and q are the model parameters. It is standard to set $n = p$, $q = 1$ [26]. The model of Hunt and Crossley has been successfully used in the analysis of a wide variety of contact/impact problems [28–31].

For simplicity, the exponents in (40) are taken as $n = p = q = 1$ for the present analysis, and the contact parameters k_c and b_c are assumed to be the same for both contacts in the model. Then, the expression of the contact forces is given by

$$\begin{Bmatrix} F_{ct} = k_c(y_t - y_p) + b_c(y_t - y_p)(\dot{y}_t - \dot{y}_p) & if\ y_t > y_p \\ F_{ct} = 0 & if\ y_t \le y_p \end{Bmatrix}. \tag{41}$$

$$\begin{Bmatrix} F_{cb} = -k_c y_b + b_c y_b \dot{y}_b & if\ y_b < 0 \\ F_{cb} = 0 & if\ y_b \ge 0 \end{Bmatrix}. \tag{42}$$

Appendix B: ***Flow of Energy in the Model***

It is illustrative to consider with some detail how energy enters and leaves the system. Clearly, the only energy input is given by the driving torque of the electric motor. This energy leaves the system in three different ways:

3. The damping term of the contact forces accounts for the energy lost due to contact and impacts between the piston and the mixture and between the mixture and the mould.
4. The nonlinear spring is also responsible for some dissipation of energy, which can be obtained as the area enclosed by the path $(\Delta L - F_m)$ followed by the spring during the process. This energy is directly related to the compaction of the mixture. Its physical interpretation may be given in terms of the viscosity associated to the flow of the resin around the grains and also the friction between quartz particles. Fig. 24 represents the whole energy dissipated by the spring during a complete compaction.
5. Damper b in Fig. 5 accounts for the energy needed to make the mixture vibrate, but not associated to the compaction itself. To understand this distinction, suppose that the slab has already been totally compacted, but the motor is still working. Then, the mixture would keep oscillating without any further compaction. Clearly, this motion has some internal damping associated, which is modelled by the linear dashpot b.

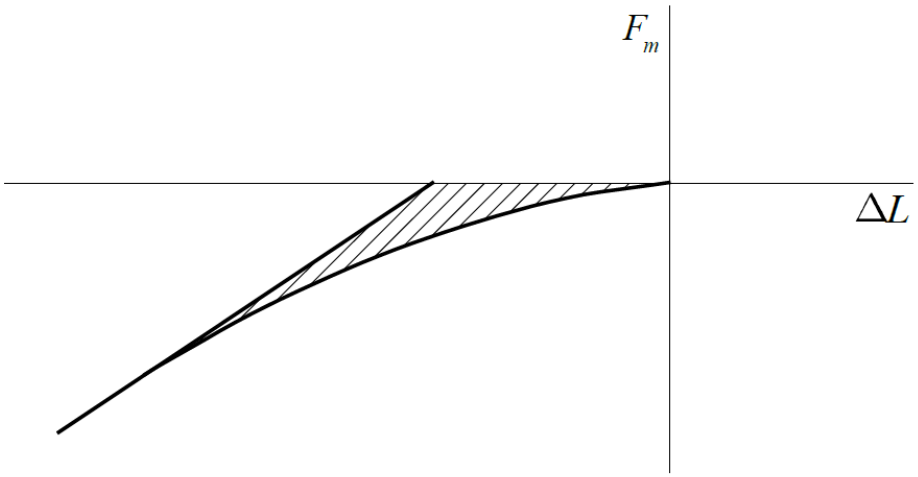

Fig. 24 Force-displacement curve of the nonlinear spring. The dashed area is the energy consumed by the nonlinear spring during a complete compaction.